Piezo-optics of GaAs

P. Etchegoin, J. Kircher,* M. Cardona, C. Grein,† and E. Bustarret‡
Max-Planck-Institut für Festkörperforschung, Heisenbergstrasse 1, D-7000 Stuttgart 80, Germany
(Received 13 May 1992; revised manuscript received 23 July 1992)

We have obtained the three independent complex components $P_{11}(\omega)$, $P_{12}(\omega)$, and $P_{44}(\omega)$ of the linear piezo-optical tensor $P_{ijkl}(\omega)$ [$\Delta\epsilon_{ij}(\omega) = P_{ijkl}(\omega)X_{kl}$] of GaAs in the ~1.5–5.4-eV photon-energy range (visible UV) by applying static uniaxial stress (**X**) along the high-symmetry directions [100] and [111] and measuring the stress-induced changes in the dielectric function $\epsilon(\omega)$. These measurements were performed using a conventional rotating analyzer ellipsometer at room temperature. The measured components of the piezo-optical tensor are in agreement with prior Kramers-Kronig analysis of piezoreflectance data. Each component of $P_{ijkl}(\omega)$ is also compared with band-structure-based calculations performed with the empirical pseudopotential method. The calculations are in reasonable agreement with the experiment. Improved deformation-potential constants D_1^1, D_1^5, D_3^3, and D_3^5 for the $E_1 - E_1 + \Delta_1$ transitions were also obtained from an analysis of the ellipsometric data. They compare favorably with theoretical estimates. In particular, the experimental value of D_3^5 agrees rather well with band-structure-based calculations, in contrast with previous measurements of this parameter.

I. INTRODUCTION AND OVERVIEW

Following our work on the piezo-optical response of germanium,[1] we present here a similar study for GaAs. Most of the experimental conditions and the analysis of data are described in Ref. 1 and redundant details will be avoided whenever possible. The effects of strain on optical properties of semiconductors are reviewed in Refs. 2–5.

The piezo-optical response of GaAs (zinc-blende-type, T_d point group) has some specific features which are absent in diamond-type semiconductors. For stress along one of the crystal axes (S_4 of T_d), the point group is reduced to D_{2d} and GaAs exhibits circular birefringence (optical activity) for light crossing the crystal with $\hat{\mathbf{k}}$ along one of the other two cubic axes (C_2' of D_{2d}).[6–9] The optical activity, however, is weak and thus only observable below the fundamental gap E_0. Even without external stress GaAs presents natural linear birefringence which is usually associated with the presence of internal strain along the specific direction of crystal growth.[10] In the visible-UV region, above the fundamental absorption edge, the piezo-optical response of GaAs is dominated by the stress-induced linear birefringence and the corresponding piezo-optical tensor (with nonvanishing real and imaginary parts) is known qualitatively from Kramers-Kronig analysis of piezoreflectance data.[11–13] However, absolute values for the so-called piezo-optical tensor are poorly known. This paper intends to fill that gap in the literature. Together with our results for Ge (Ref. 1), it illustrates the application of spectroscopic ellipsometry to the study of piezo-optical constants of semiconductors and to the evaluation of deformation-potential constants. The frequency-dependent components $P_{11}(\omega)$, $P_{12}(\omega)$, and $P_{44}(\omega)$ can be obtained in absolute units with no additional assumptions (e.g., Kramers-Kronig analysis). This is the principal advantage of piezoellipsometry with respect to piezoreflectance.

Section II of this paper discusses the experimental setup, sample preparation, data evaluation, and experimental results for both the piezo-optical components and the deformation-potential constants for the $E_1 - E_1 + \Delta_1$ transitions. Section III deals with the comparison between experiment and the empirical pseudopotential method. Section IV contains a discussion of the results.

II. EXPERIMENT

A. Experimental technique and sample preparation

The experimental technique, rotating analyzer ellipsometry (RAE), is well known to give values for the dielectric function (sometimes called pseudodielectric function if no correction for possible thin surface layers differing from the bulk is applied) with high numerical accuracy.[14,15] In addition, when the complex reflectance ratio[15,16] is analyzed with an appropriate model for the reflection process, the ellipsometric data provide a good approximation to the projection of the dielectric tensor onto the intersection of the plane of incidence and the sample surface. This was shown to be true for weakly anisotropic samples, with a large dielectric function [$|\epsilon(\omega)| \gg 1$].[17] In the present work, the complex reflectance ratio between s- and p-polarized light was converted to $\epsilon(\omega)$ using the simplest model for the reflection process, i.e., a two-phase model consisting of a sharp interface between the sample and air.

The experimental conditions were reported in our previous work on Ge; for details the reader is referred to Ref. 1. A technical description of the ellipsometer used

can be found in Ref. 18.

The samples were cut with the longest side along the high-symmetry directions [100] and [111] with typical dimensions of $18\times2.8\times1.8$ mm^3 and oriented using Laue x-ray diffraction. The bulk material used to fabricate the samples was high-purity n-type GaAs with an impurity content of less than 10^{16} cm^{-3}. Each sample was etched with 1:1 HCl:methanol (methanol rinse) as suggested previously.[19] The ellipsometric data were taken for **X** parallel and perpendicular to the plane of incidence under different stresses in increasing order up to **X**$\sim$1000 MPa. For **X** along [100] measurements were performed on the (100) face, while for **X** along [111] they were obtained on the (211) face. The different linear combinations of $P_{ij}(\omega)$'s found for each configuration for $\Delta\epsilon(\omega)$, either parallel or perpendicular to the stress, are given in Ref. 5. The results are summarized in Table I of Ref. 1. Each spectrum was corrected numerically for the presence of an oxide layer as described in Refs. 1 and 19. The thickness of the oxide layer was evaluated in each case using a three-phase model (substrate/oxide/air) and comparing our data in a region $\sim$1 eV around E_2 with the data for a very clean bare surface given in Ref. 19. The assumption of an amorphous film with the dielectric function of the electrochemically grown GaAs oxide (Ref. 20) forming the oxide layer is appropriate for mechanically polished and etched surfaces. For the photon energy region of interest here we used the dielectric function of this GaAs oxide given in Ref. 20 in order to correct for the presence of the film following the procedure reported in Ref. 1.

B. Data evaluation

When going from diamond-type semiconductors, like Si or Ge (O_h point group), to zinc-blende-type ones, like GaAs (T_d), very little has to be changed in order to analyze the piezo-optical response.[21–23] Although the symmetry of zinc blende is lower than that of diamond, both materials can be treated as a fcc lattice with a basis; both point groups (O_h and T_d) require the presence of only three independent piezo-optical constants labeled in the same way for both crystal structures.[24] These crystals when stressed along [100] or [111] become uniaxial and, to first order in the stress (**X**), the change in the second-rank dielectric tensor $\epsilon_{ij}(\omega)$ is diagonal with respect to any sets of axes which include the direction of the stress.[1,25,26] The case of a general stress (X_{ij}) (or, alternatively, strain) is described by the linear piezo-optical tensor $P_{ijkl}(\omega)$ which satisfies $P_{ijkl}=P_{jikl}=P_{ijlk}=P_{mn}$; $m,n=1,\ldots,6$ ($i=j=1\rightarrow m=1; i=1,j=2\rightarrow m=6$ and appropriate index permutations).[26] We use the definition[1]

$$\Delta\epsilon_{ij}(\omega)=P_{ijkl}(\omega)X_{kl} \tag{1}$$

for the linear piezo-optical tensor, where X_{ij} is the second-rank stress tensor, and $\Delta\epsilon_{ij}(\omega)$ the corresponding change in the complex dielectric tensor. Once $\Delta\epsilon_{ij}(\omega)$ is known, several related optical responses can be calculated. In particular, changes in the reflectivity can be directly compared with experimental piezoreflectance results which can be easily obtained from the real and imaginary parts of $\Delta\epsilon(\omega)$ using the so-called Seraphin coefficients $\alpha(\omega)$ and $\beta(\omega)$; i.e.,[27]

$$\frac{\Delta(R^{\parallel,\perp}(\omega))}{R(\omega)}=\alpha(\omega)\Delta(\mathrm{Re}[\epsilon^{\parallel,\perp}(\omega)]), \\ +\beta(\omega)\Delta(\mathrm{Im}[\epsilon^{\parallel,\perp}(\omega)]), \tag{2}$$

where $\parallel$ and $\perp$ mean parallel and perpendicular to the applied stress, respectively. It is also possible to decompose the piezo-optical tensor $P_{ij}(\omega)$ into three components belonging to different irreducible representations of the point group. These are a one-dimensional representation [hydrostatic component, $P_{11}(\omega)+2P_{12}(\omega)$] transforming like Γ_1, a two-dimensional one [$P_{11}(\omega)-P_{12}(\omega)$] which transforms like Γ_{12}, and a three-dimensional one [$P_{44}(\omega)$] transforming like Γ_{15}. Since we measure the changes in the parallel and perpendicular components of $\epsilon(\omega)$ for **X** either along [001] or [111], four linear combinations of $P_{ij}(\omega)$'s are obtained experimentally. Therefore, one of them is a linear combination of the others since $P_{ij}(\omega)$ has only three independent components. The fourth measurement can be used as a self-consistency check.[1] Kramers-Kronig consistency for the real and imaginary part of each component of $P_{ij}(\omega)$ is also expected since the piezo-optical tensor plays the role of a linear susceptibility. We investigated such consistency numerically using the experimental data with no extrapolation at lower and higher energies. An extensive comparison with previous experimental results obtained with other techniques as well as self-consistency checks are given in the following section.

The procedure followed for the evaluation of the deformation-potential constants of the $E_1-E_1+\Delta_1$ transitions is identical to that reported in Ref. 1. Here we summarize the basic facts. We use the same symbols and definitions of Ref. 1 throughout the work for consistency. The $E_1-E_1+\Delta_1$ structure in zinc-blende and diamondlike semiconductors arises from optical transitions between the valence and conduction bands along $\Lambda\langle111\rangle$.[28,32–39] The type of the optical critical points involved depends on the different curvatures of the bands along three mutually perpendicular directions. One finds[35,36,38,39] that both E_1 and $E_1+\Delta_1$ can be best modeled with a two-dimensional (2D) joint density of states. The model dielectric function as well as its second derivatives were given in Ref. 1 [Eqs. (3)–(5) of Ref. 1]. The microscopic interpretation of these features and their dependence on stress is as follows:

1. **X** $\parallel$ [100]. The effective Hamiltonian for E_1 and $E_1+\Delta_1$ for this case has been given in Refs. 40 and 41. A phenomenological exchange interaction between electron and hole Wannier functions has to be included in the Hamiltonian to explain the difference between measurements of $\epsilon(\omega)$ along and perpendicular to the stress. The eigenvalues for E_1 and $E_1+\Delta_1$ as a function of the stress can be obtained from Ref. 1 [Eqs. (7) and (8)]; they are also given in Ref. 11. From measurements of $\epsilon^{\parallel}(\omega)$ and $\epsilon^{\perp}(\omega)$ while **X** $\parallel$ [100] one obtains the hydrostatic deformation potential D_1^1 and also D_3^3 which represents the intraband effect of a [100] shear. The spin-exchange

terms are obtained by comparing the differences of $E_1(\mathbf{X})$ and $(E_1+\Delta_1)(\mathbf{X})$ found for $\epsilon(\omega)$ parallel and perpendicular to $\mathbf{X}$. The stress dependence of the amplitudes (or strengths) for both critical points has been also reported in Ref. 1 [Eqs. (15)–(18) of Ref. 1]. Of particular importance is the dependence on $\mathbf{X}$ of the ratio of a pair of amplitudes which is then independent of the absolute oscillator strengths. Unlike the eigenvalues for E_1 and $E_1+\Delta_1$ the strengths of the transitions are linear in $D_3^{3,1}$ and can be used not only to evaluate the correct sign of this deformation potential but also to check the magnitude obtained from the fit of the eigenvalues. The amplitude ratio $I_{E_1}/I_{E_1+\Delta_1}$ at $\mathbf{X}$=0 can be compared with theoretical calculations reported in Ref. 24:

$$I_{E_1}(0)/I_{E_1+\Delta_1}(0) \simeq \frac{(E_1+\Delta_1/3)(E_1+\Delta_1)^2}{(E_1)^2(E_1+2\Delta_1/3)}. \quad (3)$$

The intensity ratio given by (3) underestimates in general the experimental value but can be improved by adding the linear terms in $\mathbf{k}$, as discussed in Ref. 43.

2. $\mathbf{X} \parallel [111]$. The effective Hamiltonian for this configuration is also reported in Refs. 40 and 41. The corresponding eigenvalues and strengths as a function of $\mathbf{X}$ are in Ref. 1 [Eqs. (9)–(12) and (19)–(22) of Ref. 1]. In this case the stress fixes a preferential direction (singlet) along the stress. The three other valleys along $[\bar{1}\,\bar{1}1]$, $[\bar{1}1\bar{1}]$, and $[1\bar{1}\,\bar{1}]$ are equivalent and give rise to different eigenvalues (triplet). The parallel component of $\epsilon(\omega)$ to $\mathbf{X}$ comes from the contribution of the triplet only, and is more easy to analyze. Knowing the hydrostatic deformation potential D_1^1 from measurements with $\mathbf{X}\parallel$ [100] it is possible, in this new configuration, to obtain the deformation potentials D_5^1 (intervalley effect of a [111] shear) and D_3^5 (intravalley effect in the valence bands). D_3^5 is usually obtained from the $\mathbf{X}$ dependence of the ratio of strengths for the triplet[1] $I^T_{E_1}/I^T_{E_1+\Delta_1}(\mathbf{X})$ because the experimental points for the eigenvalues usually mask the quadratic contribution proportional to D_3^5. More details of the data evaluation are given in the following subsection.

C. Experimental results

In Fig. 1 we show typical measured spectra of the complex dielectric constant of GaAs at $\mathbf{X}$=0. The data were corrected for the presence of an oxide layer of ~12 Å. The solid symbols represent data from Ref. 19, obtained with a bare surface in N_2 atmosphere within a windowless etching cell. As for the case of Ge, we found good agreement with the data of Ref. 19, except for minor differences near $E_1 - E_1+\Delta_1$ arising from different polishing procedures of the surface. These differences have negligible effects in the evaluation of $P_{ij}(\omega)$ and the deformation-potential constants as we show below. Figure 2 displays in detail the behavior of $\epsilon_2^{\parallel}(\omega)$ for $\mathbf{X}\parallel[001]$ at three different compressive stresses around the $E_1 - E_1+\Delta_1$ transitions. In the next subsection we will show that D_3^3 is negative and, according to Eqs. (15) and (16) of Ref. 1, $\epsilon_2(\omega)$ (which is proportional to the amplitude of the transitions) should increase for E_1 and decrease for $E_1+\Delta_1$, in qualitative agreement with the

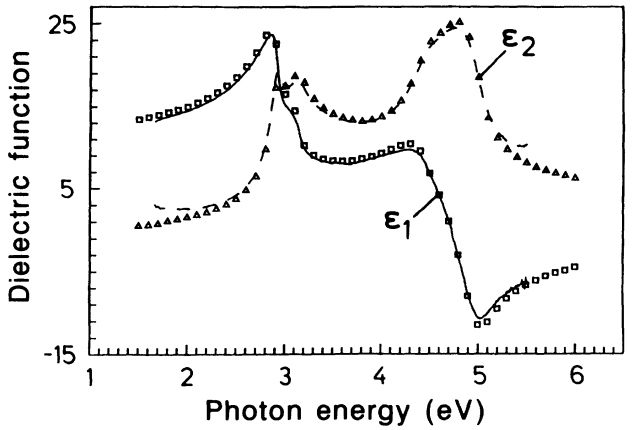

FIG. 1. Real (ϵ_1) and imaginary (ϵ_2) parts of the dielectric function of GaAs at $\mathbf{X}$=0. Solid symbols represent data tabulated in Ref. 19 for a bare surface. The solid lines are our experimental values with a correction for the presence of an oxide layer of ~12 Å.

data of Fig. 2. For a fixed photon energy, the evolution of the real and imaginary parts of $\epsilon(\omega)$ is linear up to ~600 MPa, except close to critical point transitions. An example of the nonlinearity found close to a critical point in $\epsilon_2(\omega)$ is given in the inset of Fig. 2. Using fits to the linear portions of the $\epsilon(\mathbf{X})$ dependence we obtained the corresponding linear combination of $P_{ij}(\omega)$'s discussed in Ref. 1. The three independent components of $P_{ij}(\omega)$ in the photon energy region ~1.6–5.4 eV are shown in Figs. 3(a)–3(c). The real parts of each component are plotted in Fig. 3 together with the corresponding curve obtained by Kramers-Kronig transformation of the experimental imaginary part. This curve was calculated numerically using[1]

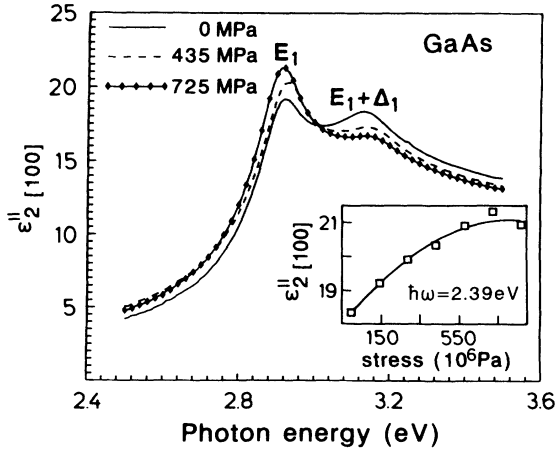

FIG. 2. Imaginary part of $\epsilon(\omega)$ as a function of the compressive stress $\mathbf{X} \parallel$ [100] in a region near $E_1 - E_1+\Delta_1$. The inset shows the evolution of $\epsilon_2(\omega)$ for a fixed photon energy as a function of the stress. Note the nonlinearities induced by the stress at $\hbar\omega \sim 2.93$ eV when $\mathbf{X} > 550$ MPa.

$$\mathrm{Re}[P_{ij}(\omega)] = \left(\frac{2}{\pi}\right) P \int_{\omega_i}^{\omega_f} \frac{\Omega\,\mathrm{Im}[P_{ij}(\Omega)]}{(\omega^2 - \Omega^2)} d\Omega + C', \qquad (4)$$

where ω_i and ω_f are the initial and final experimental energies, P means "Cauchy principal part," and C' is an *ad hoc* constant fixed so as to obtain the best fit with the directly determined $\mathrm{Re}[P_{ij}(\omega)]$. As for Ge,[1] no attempt was made to continue the frequency dependence of $P_{ij}(\omega)$ below ω_i and above ω_f since most of these contributions are being taken care of by the dispersionless parameter "C'." In addition, we have included in the inset of Figs. 3(a)–3(c) the imaginary parts of each $P_{ij}(\omega)$ obtained in arbitrary units from piezoreflectance measurements.[12] Both the Kramers-Kronig self-consistency and the quali-

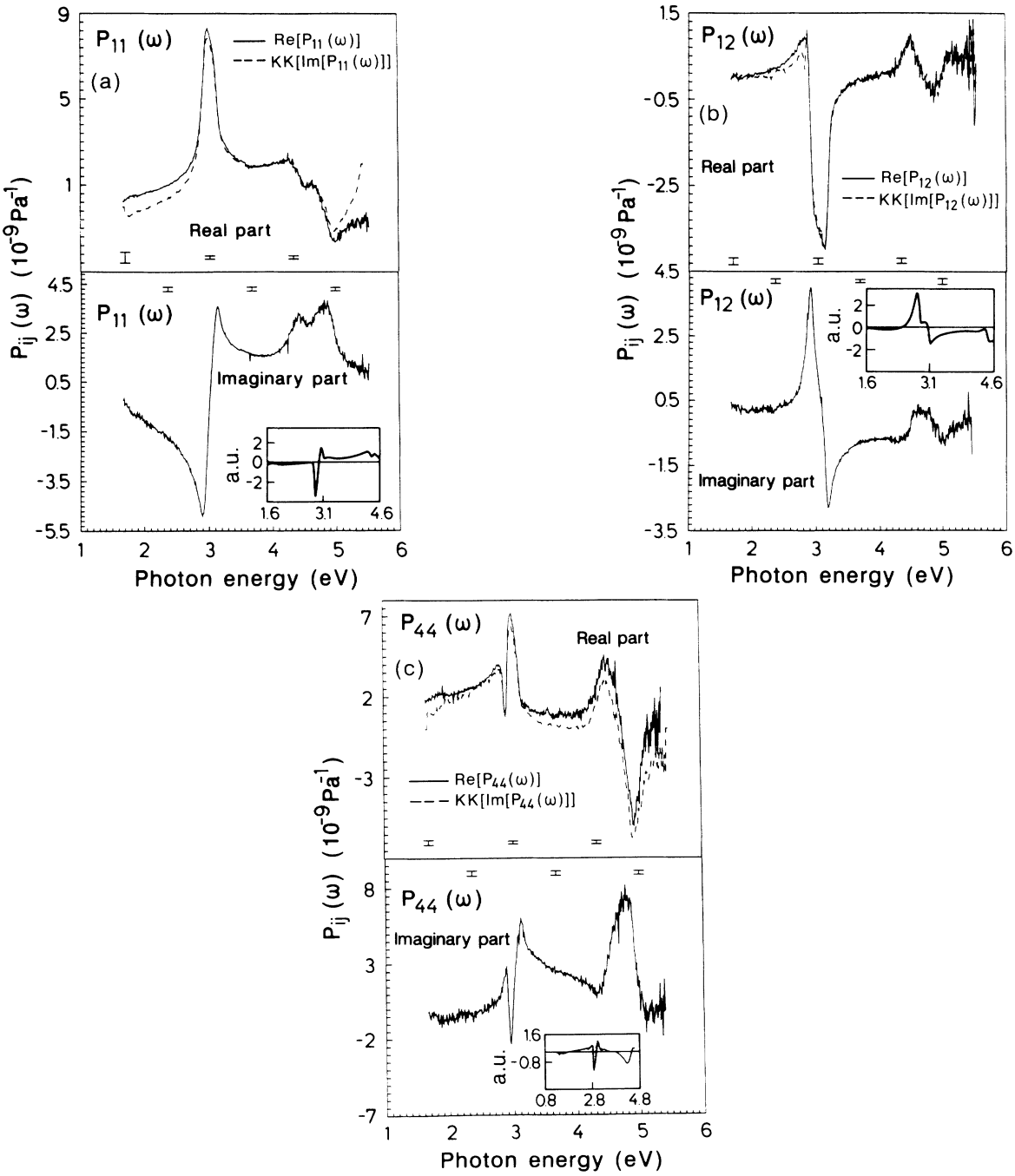

FIG. 3. (a) $P_{11}(\omega)$, (b) $P_{12}(\omega)$, and (c) $P_{44}(\omega)$ in the $\sim 1.6 - 5.4$-eV photon-energy range. On top of each figure the real part of the component is shown together with the Kramers-Kronig consistency check calculated with (4) from the imaginary part obtain in the experiment. The error bars in each case correspond to that particular photon energy. The imaginary part is shown together with the corresponding qualitative result of piezoreflectance from Ref. 12 (inset).

tative comparison with piezoreflectance data are in excellent agreement with our experimental results. The error bars in Fig. 3 were calculated as in Ref. 1; by assuming a statistical error of $\sim 10^{-2}$ for $\epsilon_{1,2}(\omega)$ (determined experimentally), and calculating the corresponding error for the slope of the linear fit of $\epsilon(\omega, \mathbf{X})$ at each ω. $P_{11}(\omega)$ and $P_{12}(\omega)$ were obtained using (Table I in Ref. 1)

$$P_{11}(\omega) = \frac{\Delta\epsilon^{\parallel}(\omega)}{\Delta \mathbf{X}_{\parallel[001]}},$$
$$P_{12}(\omega) = \frac{\Delta\epsilon^{\perp}(\omega)}{\Delta \mathbf{X}_{\parallel[001]}}, \tag{5}$$

while $P_{44}(\omega)$ was obtained from

$$P_{44}(\omega) = 2\frac{[\Delta\epsilon^{\parallel}(\omega) - \Delta\epsilon^{\perp}(\omega)]}{\Delta \mathbf{X}_{\parallel[111]}}. \tag{6}$$

In Fig. 4 we show two irreducible components of the linear piezo-optical tensor $P_{ij}(\omega)$ calculated using the data of Figs. 3(a) and 3(b). Figure 4(a) displays $[P_{11}(\omega) - P_{12}(\omega)]$, the component which transforms like Γ_{12} while Fig. 4(b) shows $[P_{11}(\omega) + 2P_{12}(\omega)]$, the hydrostatic component of the piezo-optical tensor (Γ_1).[24] In both cases the imaginary part is compared again with the corresponding piezoreflectance measurements, in arbitrary units.[12]

Using (2) it is possible to calculate $[1/R(\omega)] \times [dR(\omega)/d\mathbf{X}]$, which is expected to be proportional to the directly measured piezoreflectance spectrum $\propto [\Delta R(\omega)/R(\omega)]$. We have calculated the changes in the parallel and perpendicular components of the reflectivity with respect to the stress for both cases, $\mathbf{X}\|[001]$ and $\mathbf{X}\|[111]$, and displayed the results in Figs. 5 and 6. The insets represent again piezoreflectance data from Ref. 12.

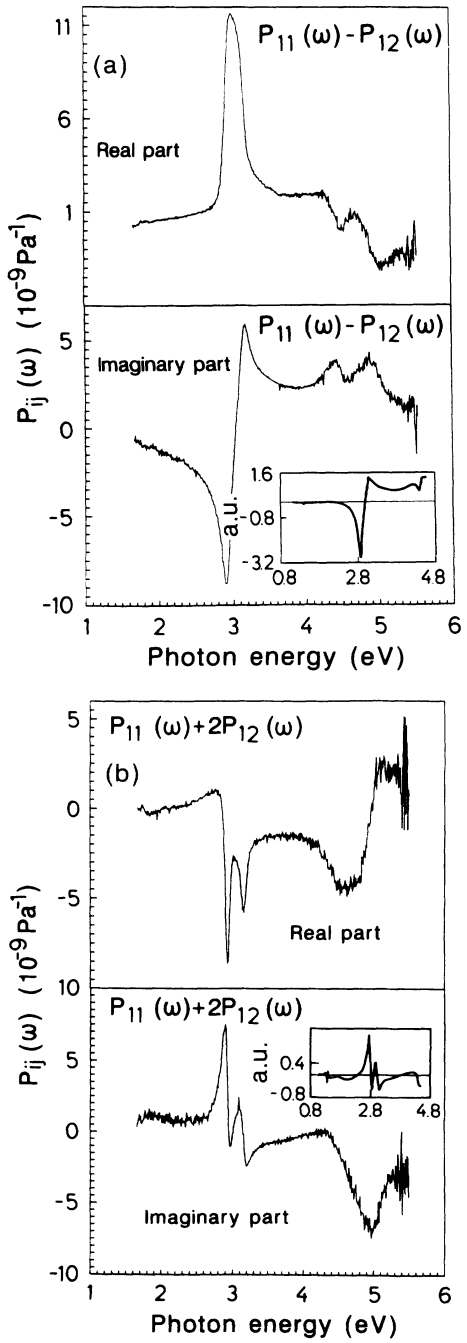

FIG. 4. (a) Γ_{12}-like and (b) Γ_1-like irreducible components of the linear piezo-optical tensor $P_{ij}(\omega)$ calculated using the data of Fig. 3 (see text for details). The imaginary parts are compared with piezoreflectance measurements from Ref. 12 in arbitrary units as in Fig. 3.

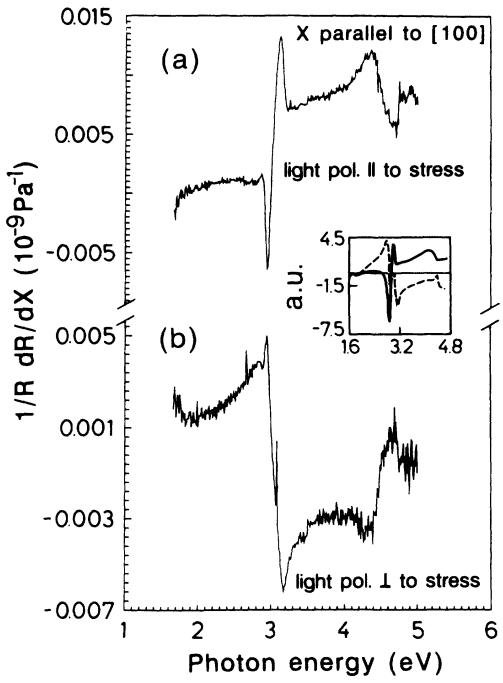

FIG. 5. Calculated derivatives of $R(\omega)$ (normalized by the reflectivity) for $\mathbf{X}\|[100]$ (or equivalent directions). (a) $[1/R(\omega)][dR(\omega)/d\mathbf{X}]$ from $\Delta\epsilon^{\parallel}(\omega)$ and (b) from $\Delta\epsilon^{\perp}(\omega)$. The inset shows data for light polarized parallel (solid line) and perpendicular (dashed line) to the stress in piezoreflectance from Ref. 12.

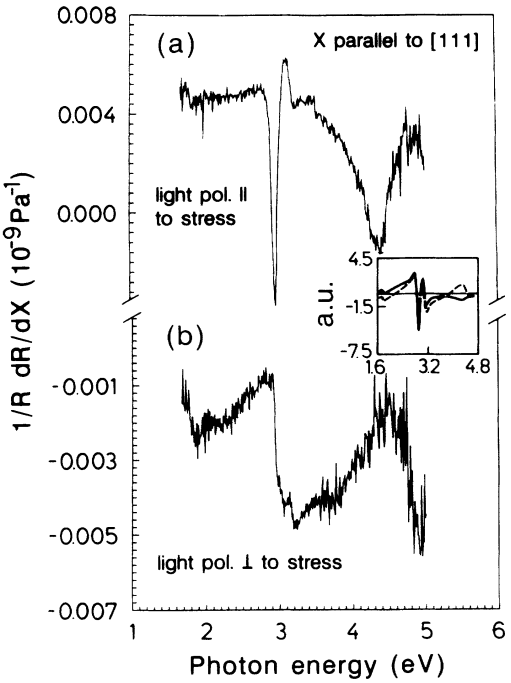

FIG. 6. Same as Fig. 5 for $\mathbf{X}\|[111]$.

Excellent agreement between both sets of results is observed.

In Fig. 7 we show the calculated reflectivity using the $\epsilon(\omega)$ values for an unstressed sample (see Fig. 1) and for one stressed along either [001] or [111], with $\mathbf{X}$=435 MPa in both cases. These data are in reasonable agreement with what is expected for $E_1 - E_1 + \Delta_1$.[1,44]

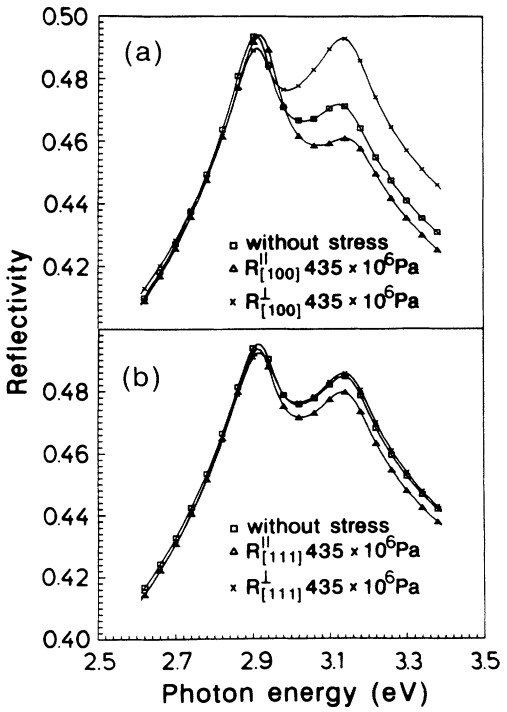

FIG. 7. Reflectivity changes calculated using the ellipsometric data for both $\mathbf{X}\|[100]$ and $\mathbf{X}\|[111]$ (see text for details) (Refs. 1 and 44).

D. Deformation-potential constants for the $E_1 - E_1 + \Delta_1$ transitions

In this subsection we discuss the critical point analysis for the $E_1 - E_1 + \Delta_1$ transitions. The error bars represent only the errors of the fits. Each parameter (amplitude, energy threshold, and broadening) is given for a confidence >96% by our fitting procedure. The trial values to start the fits were obtained from Ref. 45.

1. $\mathbf{X}\|[001]$. Figure 8 displays the dependence on stress of the E_1 and $E_1 + \Delta_1$ critical point energies as obtained from the fits with Eqs. (5) and (6) of Ref. 1. The four curves should be represented by Eqs. (7) and (8) of Ref. 1. The inset shows the same results obtained from piezoreflectance in Ref. 11. Note the different curvature of $E_1^{\|}$ with respect to the data of the inset; correspondingly, we obtained a larger absolute value of D_3^3; we shall return to this point in the discussion of the results. D_1^1 was evaluated from $\frac{1}{2}(\overline{E_1} + \overline{E_1 + \Delta_1})$,[1] which is independent of δ_{J_1}, δ_{J_2}, and D_3^3. The results are plotted in Fig. 9(a). Two values for D_3^3 were obtained, from $\frac{1}{2}(E_1^{\|} + E_1^{\perp})$ and $\frac{1}{2}[(E_1+\Delta_1)^{\|} + (E_1+\Delta_1)^{\perp}]$, respectively, as displayed in Figs. 9(b) and 9(c). These are curves which are independent of δ_{J_1} and δ_{J_2}. The reader is referred to Ref. 1 for details. Using the so-obtained values for D_1^1 and D_3^3 we can obtain $\delta_{J_{1,2}}$ and compare the ratio of amplitudes with theoretical predictions. In Fig. 10 we show the amplitude ratios for both E_1 and $E_1 + \Delta_1$. The curves were calculated from the ratios of Eqs. (15) to (16), and (17) to (18) of Ref. 1 with the value for D_3^3 previously obtained (see above). In Fig. 10 not only the absolute value of D_3^3 is checked but also the correct sign of this

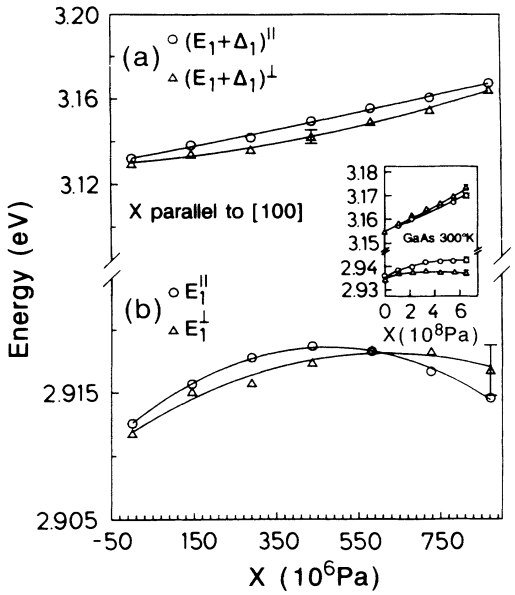

FIG. 8. $E_1^{\|,\perp}$ and $(E_1 + \Delta_1)^{\|,\perp}$ as a function of the stress for $\mathbf{X}\|[100]$ (or equivalent directions). The inset shows data from Ref. 11 obtained with a critical point analysis of the piezoreflectance data. The same symbols are used in order to compare with our experiments.

deformation potential can be determined. All the values of the deformation-potential constants and spin-exchange parameters so obtained are given in Table I.

2. $\mathbf{X}\|[111]$. As done for Ge,[1] we analyze $\Delta\epsilon^{\|}(\omega)$ which has contributions from the triplet only. However, we display in Fig. 11 the complete set of data for the components parallel and perpendicular to $\mathbf{X}$ for both E_1 and $E_1+\Delta_1$ and compare them with the data of Ref. 11 (inset). The differences between our results and those of Ref. 11 lead to a different value for D_3^5. Anticipating the discussion of results we mention that our value is in better agreement with theoretical estimates than that of Ref. 11. In Fig. 12(a) we show the average $\frac{1}{2}[E_1^T+(E_1+\Delta_1)^T]$ which, according to Eqs. (11) and (12) of Ref. 1, is independent of D_3^5 and can be fitted to a straight line to obtain D_1^5, using the previously obtained D_1^1 (hydrostatic deformation potential). D_3^5 cannot be obtained from either E_1^T or $(E_1+\Delta_1)^T$ in Fig. 11 because of the small curvature masked by the linear portion and the experimental uncertainties.[1] D_3^5 was obtained from the fit of $I_{E_1}^T/I_{E_1+\Delta_1}^T$ vs $\mathbf{X}$, given by the ratio of Eqs. (19) and (20) of Ref. 1. Since D_3^5 is small, that ratio can be approximated by a linear function of $\mathbf{X}$; Fig. 12(b) shows the

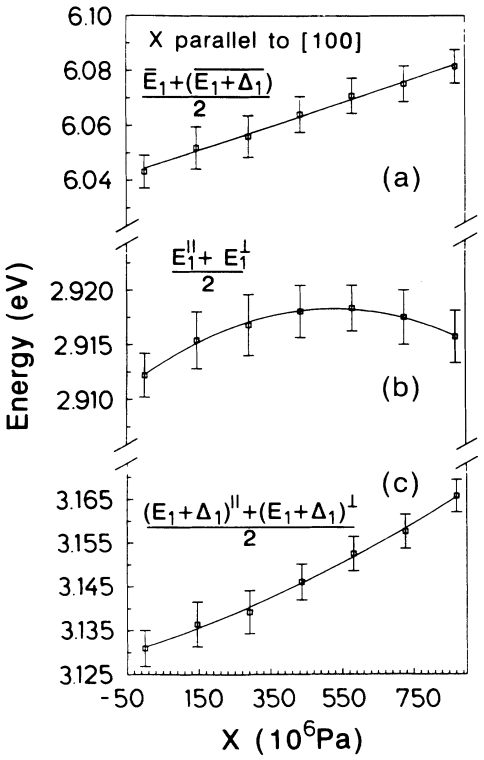

FIG. 9. (a) $\frac{1}{2}[\overline{E_1}+(\overline{E_1+\Delta_1})]$. The experimental values can be fitted to a line to obtain D_1^1 (hydrostatic deformation potential) (Ref. 42). (b) and (c) correspond to the average between the parallel and the perpendicular results for E_1 and $E_1+\Delta_1$ of Fig. 8 which are independent of the exchange terms $\delta J_{1,2}$. Fitting both with a parabola, it is possible to obtain two independent values of $|D_3^3|$ (Ref. 1). All the numerical values obtained in the fits are given in Table I. The sign of D_3^3 has to be determined using the data of Fig. 10.

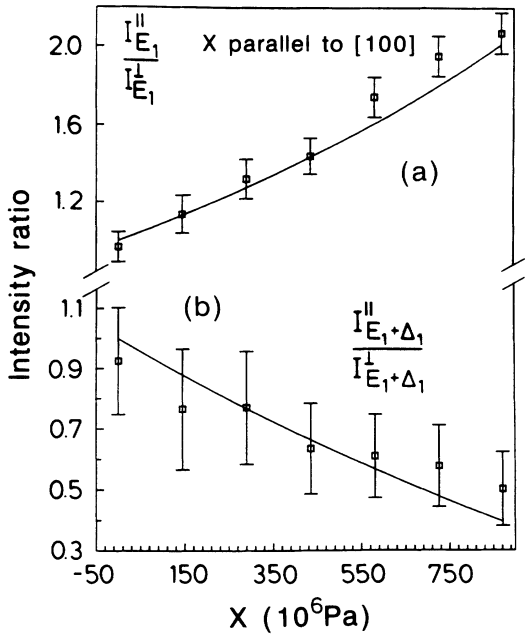

FIG. 10. (a) Intensity ratios obtained from the fits of the experimental data with Eqs. (5) and (6) of Ref. 1. The solid line is the ratio of Eq. (15) to (16) in Ref. 1 with the value of D_3^3 obtained above (Fig. 9). From this plot the sign of D_3^3 can be determined. (b) Same as (a) but for the $E_1+\Delta_1$ transition. The solid line is the ratio of Eq. (17) to (18) in Ref. 1.

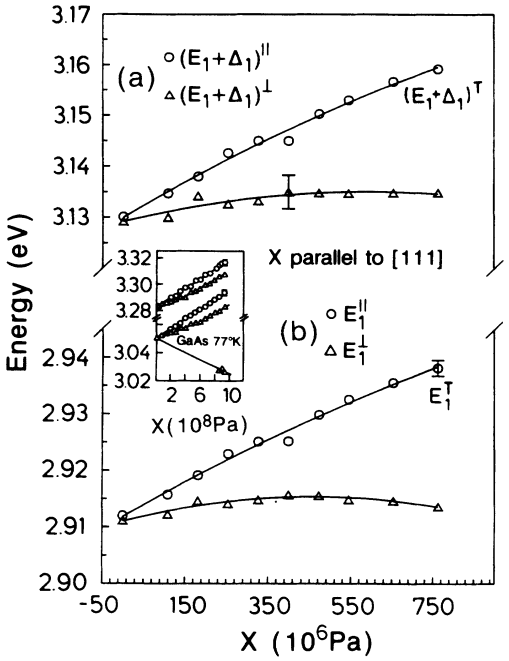

FIG. 11. (a) $(E_1+\Delta_1)^{\|,\perp}$ and (b) $(E_1)^{\|,\perp}$ for $\mathbf{X}\|[111]$. In both cases the parallel component has only contributions from the triplet. The inset shows data from Ref. 11. The differences between the curvatures of the plots shown in the inset and our experimental data are related to different values for D_3^5 (see Table I). The inset from Ref. 11 included three points indicating the contributions of the singlet (lowest curve) which we do not separate out in our data.

TABLE I. Deformation-potential constants and spin-exchange parameters (in eV) for the $E_1 - E_1 + \Delta_1$ transitions in GaAs, compared to other measurements and theoretical results.

D_1^1	D_1^5	D_3^3 (eV)	D_3^5 (eV)	δ_{J_1} (meV)	δ_{J_2} (meV)	Ref.
$-7.6 \pm 0.5^{a,c}$	$9.2 \pm 0.9^{a,c}$	$3.4 \pm 0.3^{b,c,j}$	$0 \pm 0.5^{a,c}$	$10.2 \pm 1.0^{b,c,e}$	$5.5 \pm 0.8^{b,c,g}$	11, 40
$-7.9 \pm 0.5^{b,c}$		$3.5 \pm 0.3^{b,d,j}$		$9.9 \pm 1.0^{b,d,e}$	$3.6 \pm 0.5^{b,d,g}$	11, 40
$6.7 \pm 0.5^{b,d}$						11, 40
-6.9 ± 0.7^{i}	6.2 ± 0.6^{i}					47
-9.4 ± 0.9^{d}	8.5 ± 0.8^{d}	2.4 (at $\mathbf{k} = 0$)^{j}	8.5 (at $\mathbf{k} = 0$)^{j}			13
-8.0 ± 0.8^{d}		$3.2 \pm 0.3^{c,j}$		$10^{c,e}$	$10^{c,e}$	41
-9.3						48
-14.4^{h}	7.9 ± 0.5^{h}					49
	$12.5^{h}(\zeta = 0.76)$		$-6^{h}(\zeta = 0.76)$			30
	$12.3^{h}(\zeta = 0.6)$		$-4.5^{h}(\zeta = 0.6)$			30
$-8.4 \pm 0.8^{d,e,f}$	$12.0 \pm 0.7^{d,e,f}$	$-5.4 \pm 0.9^{d,e}$	$-6.4 \pm 1.5^{d,g}$	8.0 ± 1.5^{d}	6.1 ± 1.2^{d}	present work
		$-4.3 \pm 0.8^{d,f}$				present work

[a] $X \parallel [111]$.
[b] $X \parallel [001]$.
[c] 77 K.
[d] 300 K.
[e] E_1 peak.
[f] $E_1 + \Delta_1$ peak.
[g] $I^{\parallel}_{E_1}/I^{\parallel}_{E_1+\Delta_1}$ for $\mathbf{X}\parallel[111]$.
[h] Theory; see Fig. 15 and text.
[i] 2 K.
[j] Absolute value.

best linear fit to the data. All the deformation-potential constants obtained from these fits are also given in Table I.

The intensity ratio given in (3) predicts $I_{E_1}(0)/I_{E_1+\Delta_1}(0) \sim 1.13$, for $\mathbf{X}$=0, which agrees rather well with the experimental ratio (see Fig. 10), especially in view of the fact that linear terms in $\mathbf{k}$ have not been considered in (3).[43]

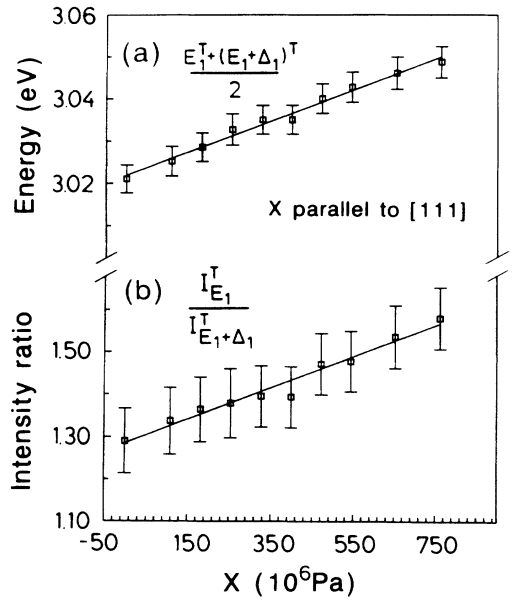

FIG. 12. (a) $\frac{1}{2}[E_1^T + (E_1 + \Delta_1)^T]$ as a function of $\mathbf{X}$. The data were obtained by analyzing the change in $\Delta\epsilon^{\parallel}(\omega)$ which has contributions from the triplet only. (b) Intensity ratio [Eqs. (19) and (20) in Ref. 1] for the triplet. From the linear fit of this curve we obtained the value (and correct sign) for D_3^5 that is displayed in Table I.

III. PSEUDOPOTENTIAL CALCULATIONS

In this section we deal with the predictions of the empirical pseudopotential method[22] (EPM) for the different components of the piezo-optical tensor $P_{ij}(\omega)$. We used the same computer code that was employed for Ge in Ref. 1. We computed the imaginary part of $\epsilon(\omega)$ using

$$\epsilon_2(\omega) = \frac{4\pi^2 e^2 \hbar}{3m^2\omega^2} \sum_{c,v} \frac{2}{(2\pi)^3} \int_{\mathrm{BZ}} |\langle u_{i,\mathbf{k}} | \nabla | u_{j,\mathbf{k}} \rangle|^2 \times \delta(E_c(\mathbf{k}) - E_v(\mathbf{k}) - \omega) d\mathbf{k} \quad (7)$$

and a Lorentzian with a broadening $\Gamma_0 \sim 0.1$ eV to simulate the $\delta(E)$ function. For the stressed lattice we interpolated the well-known symmetric and antisymmetric form factors $V_S(\mathbf{G})$ and $V_A(\mathbf{G})$ (Refs. 22 and 29) ($\mathbf{G}^2 = 3, 4, 11$) ($\mathbf{G}$ is a reciprocal-lattice vector in units of $2\pi/a$) to obtain the new Fourier components of the pseudopotential using the approach sketched in Ref. 1. For $\mathbf{X}\parallel[111]$ the deformation of the primitive cell (internal strain) was taken into account with the internal strain parameter ζ=0.6.[30,31] We used a sampling of 2361 points within the full first Brillouin zone.[1] In Fig. 13 we show the imaginary part of the dielectric function $\epsilon_2(\omega)$ evaluated with (7) for the unstressed lattice. The inset shows $\epsilon_2(\omega)$ calculated in Refs. 29 and 23. Our calculation as well as the one shown in the inset represent poorly the experimental imaginary part of the dielectric function around E_1. This is expected for a one-electron type

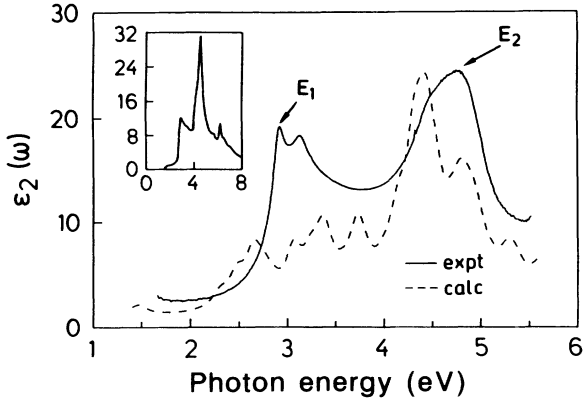

FIG. 13. Experimental (solid) and calculated (dashed) imaginary part of the dielectric function for $\mathbf{X}$=0. The inset shows an EPM calculation reported in Ref. 29. The EPM calculation is particularly far from the experiment near $E_1 - E_1 + \Delta_1$ where the excitonic contributions are known to play an important role. The low density of $\mathbf{k}$ points within the first BZ introduces the artificial structure between $(E_1 - E_1 + \Delta_1)$ and (E_2). However, the so-calculated $\epsilon_2(\omega)$ still reproduces the $P_{ij}(\omega)$'s moderately well.

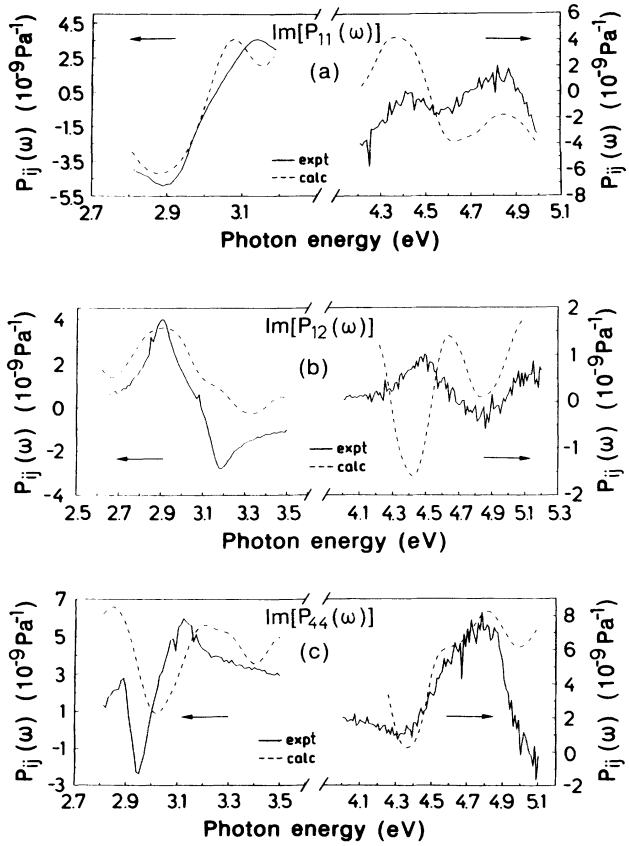

FIG. 14. Experimental (solid) and calculated (dashed) imaginary parts of the piezo-optical constants (a) $P_{11}(\omega)$, (b) $P_{12}(\omega)$, and (c) $P_{44}(\omega)$ (see text for details).

of calculation: exciton effects are known to sharpen and increase the weight of these structures thus improving agreement with experiment. However, the EPM method reproduces differential effects quite well,[46] in particular those in which the excitonic character of the critical points does not change as a function of the external modulation. In the case of Ge,[1] we found that the EPM method describes reasonably well the components of the piezo-optical tensor near the critical points $E_1 - E_1 + \Delta_1$ and E_2 although the explicit calculation of $\epsilon_2(\omega)$ had the same problems as here. In Fig. 14 we show the three independent components of the piezo-optical tensor $P_{ij}(\omega)$ calculated with the EPM near the optical critical points $E_1 - E_1 + \Delta_1$ and E_2. Despite the fact that the calculation did not include spin-orbit coupling, the general shape of the piezo-optical components are in good agreement with the experimental determination. The calculated values near E_2 are in absolute units while those near $E_1 - E_1 + \Delta_1$ were multiplied by a factor of ~ 1.9 so as to exhibit approximately the same amplitude as the experiment. The theoretical values were obtained from the difference between $\epsilon_2(\omega)$ for $\mathbf{X}$=0 and a calculation for $\mathbf{X}$=2.4 GPa along either [001] or [111]. As in the case of Ge,[1] we had to use an unrealistic value for the stress, in comparison to those used in the experiment, to avoid numerical problems with small differences. The lack of spin-orbit coupling eliminates some of the sources of nonlinearities and the so-obtained components of the piezo-optical tensor still show general agreement with the experimental data.

IV. DISCUSSION AND CONCLUSIONS

Our experimental data for the components of the piezo-optical tensor of GaAs were shown to be Kramers-Kronig consistent and compatible with prior results obtained by

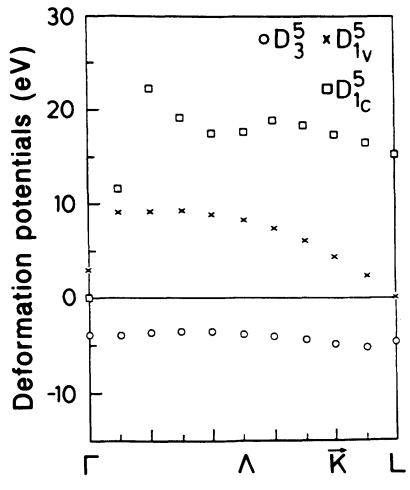

FIG. 15. Deformation-potential constants D_3^5 and D_1^5 (conduction and valence band) along ⟨111⟩ calculated with the EPM (Ref. 30) using the rigid-ion-pseudopotential obtained by interpolation of the empirical pseudopotential form factors of Ref. 50. These results correspond to an internal strain parameter ζ=0.6.

Kramers-Kronig analysis of piezoreflectance experiments. Numerical processing allowed us to compare our results with those of direct piezoreflectance measurements (see Figs. 5 and 6); this comparison is quite satisfactory. The EPM method with no spin-orbit coupling reproduces reasonably well the experimental data. The experimental piezo-optical components $P_{ij}(\omega)$ have been given in absolute units and can be used for numerical estimates of optical properties of stressed GaAs layers in the visible, near IR, and near UV. Evaluation of the deformation-potential constants for our data shows, as in the case of Ge,[1] some differences with respect to prior work (see Table I); in particular concerning the shear deformation potential D_3^5. Our results seem to agree quite well with theoretical predictions using the EPM method. In Fig. 15 we plot the theoretical values for D_3^5 and D_1^5 (conduction and valence bands) obtained in Ref. 30 also with the EPM. The values displayed in Table I are an average from Γ to L along $\langle 111 \rangle$ for two different internal strain parameters (ζ). Our experimental determination is in better agreement with the EPM estimates than previous ones. EPM is known to yield reliable predictions of the deformation-potential constants, a fact which gives extra confidence to our experiments. In addition, the correct sign for the shear deformation-potential constants was determined from the intensity ratios of the amplitudes for E_1 and $E_1 + \Delta_1$. To the best of our knowledge there are no *ab initio* calculations in the literature to compare with our data.

A similar study for Si is in progress and will be published elsewhere.[51]

ACKNOWLEDGMENTS

Thanks are due to H. Hirt, M. Siemers, and P. Wurster for expert technical help during the experiments. The original codes to analyze the ellipsometric data were written by M. Garriga.[18] It is a pleasure to thank D. S. Citrin for a critical reading of the manuscript.

---

*Present address: Department of Physics, University of California, Berkeley, CA 74720.

†Present address: Division of Applied Sciences, Pierce Hall, Harvard University, Cambridge, MA 02138.

‡Present address: Laboratoire d'Etudes des Propriétés Electronique des Solides, CNRS, 166X, F-38042, Grenoble, France.

[1] P. Etchegoin, J. Kircher, M. Cardona, and C. Grein, Phys. Rev. B **45**, 11 721 (1992).

[2] G. L. Bir and G. E. Pikus, in *Symmetry and Strain-Induced Effects in Semiconductors*, edited by D. Louvish (Wiley, New York, 1974).

[3] E. O. Kane, Phys. Rev. **178**, 1368 (1969), and references therein.

[4] F. Pollak, Surf. Sci. **37**, 863 (1973).

[5] I. Balslev, in *Semiconductors and Semimetals*, edited by X. Willardson and X. Beer (Academic, New York, 1972), Vol. 9.

[6] P. Etchegoin and M. Cardona, Solid State Commun. **82**, 655 (1992).

[7] L. D. Landau and E. M. Lifshitz, *Electrodynamics of Continuous Media* (Pergamon, Oxford, 1963), pp. 342–343.

[8] L. E. Solov'ev and M. O. Chaĭka, Fiz. Tverd. Tela (Leningrad) **22**, 970 (1980) [Sov. Phys. Solid State **22**, 568 (1980)].

[9] L. E. Solov'ev, Opt. Spektrosk. **46**, 1020 (1979) [Opt. Spectrosc. (USSR) **46**, 575 (1979)].

[10] P. Y. Yu and M. Cardona, J. Phys. Chem. Solids **34**, 29 (1973); P. Y. Yu, Ph.D. thesis, Brown University, 1972.

[11] M. Chandrasekhar and F. Pollak, Phys. Rev. B **15**, 2127 (1977).

[12] J. E. Wells, Ph.D. thesis, University of Illinois, Urbana, 1969.

[13] F. Pollak and M. Cardona, Phys. Rev. **172**, 816 (1968).

[14] D. E. Aspnes and A. A. Studna, Rev. Sci. Instrum. **49**, 292 (1978).

[15] R. M. Azzam and N. M. Bashara, *Ellipsometry and Polarized Light* (North-Holland, Amsterdam, 1977).

[16] D. S. Kliger, J. W. Lewis, and C. E. Randall, *Polarized Light in Optics and Spectroscopy* (Academic, Boston, 1990).

[17] D. E. Aspnes, J. Opt. Soc. Am. **70**, 1275 (1980).

[18] M. Garriga, Ph.D. thesis, University of Stuttgart, 1990.

[19] D. E. Aspnes and A. A. Studna, Phys. Rev. B **27**, 985 (1983).

[20] D. E. Aspnes, G. P. Schwartz, G. J. Gualtieri, A. A. Studna, and B. Schwartz, J. Electrochem. Soc. **128**, 590 (1981).

[21] M. Cardona, in *Atomic Structure and Properties of Solids*, edited by E. Burstein (Academic, New York, 1972), p. 513.

[22] M. L. Cohen and J. R. Chelikowsky, in *Electronic Structure and Optical Properties of Semiconductors*, edited by M. Cardona, Springer Series in Solid-State Science Vol. 75 (Springer, Heidelberg, 1988).

[23] M. L. Cohen and V. Heine, in *Solid State Physics: Advances in Research and Applications*, edited by H. Ehrenreich, F. Seitz, and D. Turnbull (Academic, New York, 1970), Vol. 24, p. 142.

[24] M. Cardona, in *Light Scattering in Solids II*, edited by M. Cardona and G. Güntherodt (Springer, Berlin, 1982), Vol. 50, p. 163.

[25] A. Blacha, H. Presting, and M. Cardona, Phys. Status Solidi B **126**, 11 (1984).

[26] B. N. Grechushnikov, in *Modern Crystallography IV*, edited by H. J. Quiesser, Springer Series in Solid-State Science Vol. 37 (Springer, Heidelberg, 1988).

[27] B. Seraphin *et al.*, Phys. Rev. **145**, 628 (1966).

[28] L. Viña, S. Logothetidis, and M. Cardona, Phys. Rev. B **30**, 1979 (1984).

[29] J. P. Walter and M. Cohen, Phys. Rev. B **183**, 763 (1969).

[30] H. Presting, Ph.D. thesis, University of Stuttgart, 1985.

[31] R. M. Martin, Phys. Rev. B **1**, 4005 (1970).

[32] S. Koeppen, P. Handler, and S. Jasperson, Phys. Rev. Lett. **27**, 265 (1971).

[33] J. Humlíček, Phys. Status Solidi B **86**, 303 (1978).

[34] J. Musilová, Phys. Status Solidi B **101**, 85 (1980).

[35] M. Cardona, in *Modulation Spectroscopy*, edited by F. Seitz, D. Turnbull, and H. Ehrenreich (Academic, New York,

1966).
[36]D. E. Aspnes and J. E. Rowe, Phys. Rev. B **7**, 887 (1973).
[37]J. E. Rowe and D. E. Aspnes, Phys. Rev. Lett. **25**, 162 (1970).
[38]D. E. Aspnes, in *Handbook on Semiconductors*, edited by T. S. Moss and M. Balkanski (North-Holland, Amsterdam, 1980).
[39]D. E. Aspnes, Phys. Rev. Lett. **28**, 168 (1972); D. E. Aspnes and A. A. Studna, Surf. Sci. **96**, 294 (1980).
[40]M. Chandrapal and F. Pollak, Solid State Commun. **18**, 1263 (1976).
[41]J. E. Rowe, F. H. Pollak, and M. Cardona, Phys. Rev. Lett. **22**, 933 (1969).
[42]J. Bardeen and W. Shockley, Phys. Rev. **80**, 72 (1950).
[43]M. Cardona, N. E. Christensen, and G. Fasol, Phys. Rev. B **38**, 1806 (1988).
[44]U. Gerhardt, Phys. Rev. Lett. **15**, 401 (1965).
[45]S. Logothetidis, M. Cardona, and M. Garriga, Phys. Rev. B **43**, 11950 (1983).
[46]H. R. Philipp and H. Ehrenreich, Phys. Rev. **129**, 1550 (1963).
[47]D. D. Sell and S. E. Stokowski, in *Proceedings of the Tenth International Conference on the Physics of Semiconductors, Cambridge, 1970* (U.S. AEC, Oak Ridge, 1970), p. 417.
[48]M. I. Wolfe, Ph.D. thesis, Yeshiva University, 1973.
[49]P. J. Melz (unpublished).
[50]M. L. Cohen and T.K Berstresser, Phys. Rev. **141**, B789 (1966).
[51]P. Etchegoin, J. Kircher, M. Cardona, and C. Grein (unpublished).